

# Development of the CYGNSS Geophysical Model Function for Wind Speed

Christopher S. Ruf, *Fellow, IEEE*, Rajeswari Balasubramaniam, *Student Member, IEEE*

**Abstract**— Geophysical Model Functions (GMFs) are developed which map the Level 1 observables made by the Cyclone Global Navigation Satellite System (CYGNSS) radar receivers to ocean surface wind speed. The observables are: 1) the normalized bistatic radar cross section ( $\sigma_0$ ) of the ocean surface; and 2) the slope of the leading edge of the radar return pulse scattered by the ocean surface. GMFs are empirically derived from measurements by CYGNSS which are nearly coincident with independent estimates of the 10 meter referenced ocean surface wind speed ( $u_{10}$ ). Two different sources of “ground truth” wind speed are considered – numerical weather prediction model outputs and measurements by the NOAA P-3 hurricane hunter during eyewall penetrations of major hurricanes. The GMFs derived in each case have significant differences that are believed to result from differences in the state of development of the long wave portion of the ocean surface height spectrum that result from characteristic differences in wave age and fetch length near vs. far from a hurricane.

**Index Terms**— CYGNSS, Geophysical Model Function, GNSS-R, Ocean Surface Wind Speed

## I. INTRODUCTION

OCEAN surface wind speed can be estimated from spaceborne observations made by microwave radiometers and radars. Radiometers measure brightness temperature, from which a surface emissivity observable is derived. The sensitivity to wind results primarily from the generation of foam on the ocean surface, which has a significantly different emissivity than that of water alone [1], [2], [3]. The estimation of wind speed from the emissivity observable typically relies on a geophysical model function (GMF) which relates the two. GMFs can either be developed from a “first principles” analysis of the electromagnetics or, what is more common in practice, they can be constructed empirically by relating a large population of observations to near-coincident measurements of the wind speed made by some other means. Radars measure scattered transmitted signals, from which

observables related to the scattering properties of the surface are derived. The sensitivity to wind results primarily from the roughening of the ocean surface, which alters both the radar scattering cross section and the shape of the scattered radar waveform relative to that for a smooth water surface. A GMF approach is also often used with radar wind sensors. A GMF relating wind speed to the scattering cross section observable has been used by ocean scatterometers [4], [5]. A correction to such a GMF has been considered for ocean altimeters using additional information about the significant wave height of the ocean contained in the shape of the leading edge of the radar return waveform [6], [7].

Both scatterometers and altimeters are examples of monostatic radars, which carry a co-located transmitter and receiver and measure the backscatter signal. Another type of radar is bistatic, with transmitter and receiver in different locations. Global Navigation Satellite System-Reflectometry (GNSS-R) instruments, which make use of Global Positioning System (GPS) or other navigation signals as their transmitters, are examples of bistatic radars. Their preferred bistatic measurement geometry is quasi-specular forward scattering because the scattering cross section tends to be largest in that direction. Examples of spaceborne GNSS-R instruments which have successfully measured ocean surface winds are the UK Disaster Monitoring Constellation (UK-DMC) [8], [9] and TechDemoSat-1 (TDS-1) [10], [11], [12]. These missions have reported their wind speed retrieval performance in the literature, but not the details of the GMFs used by their retrieval algorithms. In addition, both UK-DMC and TDS-1 make measurements at lower (near nadir) incidence angles only, due to the orientation of their receive antenna beams, so their GMFs would be restricted to those angles. Sensitivity to hurricane force winds has also been demonstrated by TDS-1 [13], but a corresponding high wind GMF has not yet been reported. GNSS-R instruments have also flown on aircraft to measure ocean surface winds [14], [15].

GNSS-R radar receivers measure the scattering cross section of the ocean surface at and in a region surrounding the specular reflection point. The measurements are localized on the Earth surface using a combination of time delay and Doppler frequency filters to form a Delay Doppler Map (DDM) of the surface [16]. The time delay filter acts similarly as the range gating function in conventional monostatic radars to isolate regions on the surface with a particular time-of-flight from the transmitter to the receiver. The Doppler filter similarly isolates regions on the surface at which the GPS

Manuscript received January 31, 2018, revised April 9, 2018, accepted May 2, 2018. This work was supported in part by NASA Science Mission Directorate Contract NNL13AQ00C. (*Corresponding author: Christopher S. Ruf.*)

C. S. Ruf is with the Climate and Space Department, University of Michigan, Ann Arbor, MI 48109 USA (e-mail: cruf@umich.edu).

R. Balasubramaniam is with the Climate and Space Department, University of Michigan, Ann Arbor, MI 48109 USA (e-mail: rajibala@umich.edu).

Digital Object Identifier 10.1109/JSTARS.2018.2833075

signal experiences a particular Doppler shift. Numerous observables can be derived from a DDM for use in wind speed retrievals. For airborne applications, wind speed GMFs have been developed based on the relative strength of the scattering at and away from the specular point [17]. This makes use of the fact that specular scattering tends to decrease while diffuse scattering, away from the specular point, tends to increase as wind speed and surface roughness increase. This approach has the advantage that the observable is a ratio between two received signal strengths, so ancillary measurement parameters such as the strength of the GPS transmitted signal and the gain of the receive antenna, largely cancel out. For spaceborne applications, it is problematic to rely on this ratio-based approach because differences in time delay and Doppler shift correspond to much greater differences in distance from the specular point at satellite altitudes and orbital velocities. As a result, use of such a ratio approach could result in an effective spatial resolution of 100s of km for the derived wind speed, rather than a few km in the case of aircraft [18]. In order to maintain a spatial resolution of 10s of km, spaceborne wind speed retrievals tend to rely only on DDM measurements near the specular point [19].

The Cyclone Global Navigation Satellite System (CYGNSS) consists of a constellation of eight small satellites deployed in a common 520 km altitude, 35° inclination Earth orbit. The mission is intended to make frequent measurements of ocean surface wind speed in all precipitating conditions, in particular in and near tropical cyclones [20]. Each satellite carries a GNSS-R radar receiver, tuned to the GPS L1 signal at 1.575 GHz, which continuously generates DDMs of surface reflections from specular points within the footprints of its two downward pointing receive antenna beams [21]. The receivers are a third generation version of the Space GPS Receiver Remote Sensing Instrument (SG-ReSI) product line developed by Surrey Satellite Technology Ltd. over the past ~15 years [22]. The two CYGNSS receive antenna beams are pointed cross track to the direction of orbital motion. Each antenna is a 2x3 element phased array with a fan beam antenna pattern. The patterns cover incidence angles of approximately 5–65 deg and azimuth angles of 75–105 deg and 255–285 deg on the port and starboard sides of the sub-satellite point, respectively. DDMs are processed into two observables which are used for wind speed retrieval. One is the normalized scattering cross section ( $\sigma_o$ ) averaged over an area roughly 25 km in diameter centered on the specular point. The other is the leading edge of the slope of the radar return waveform (LES). Both observables are defined in [23], which describes the wind speed retrieval algorithm used by the CYGNSS mission and develops an initial, pre-launch, GMF based on simulated measurements.

An empirical GMF is developed here for use by the CYGNSS wind speed retrieval algorithm. It uses near-coincident matchups between the CYGNSS observables and independent estimates of the ocean surface wind speed referenced to a 10 m height ( $u_{10}$ ). The independent wind speeds are provided by Numerical Weather Prediction (NWP) models at low to moderate wind speeds and by instruments on the NOAA P-3

hurricane hunter aircraft at higher wind speeds in tropical cyclones [24]. The GMF developed here is distinct from those reported previously in two primary respects. With previous airborne applications, the observables were either uncalibrated Signal-to-Noise Ratio (SNR) measurements of the received GPS signal, or normalized measures of the extent of diffuse scattering away from the specular point. The GMF developed here instead uses as its observables the absolutely calibrated  $\sigma_o$  of the surface in the vicinity of the specular and the LES. With previous spaceborne applications, coincident matchup measurements were not available at hurricane force wind speeds from the NOAA P-3 hurricane hunter aircraft. Their availability allows for the extension of the GMF to significantly higher wind speeds than has been reported previously. The GMF development is presented in two stages. First, a Fully Developed Seas (FDS) version is developed based on matchups with NWP model outputs at low to moderate wind speeds. Then a Young Seas/Limited Fetch (YSLF) version is presented based on matchups with measurements by hurricane hunter aircraft during flights through several 2017 Atlantic hurricanes.

## II. FULLY DEVELOPED SEAS GMF

The FDS GMF is based on an empirical pairing of CYGNSS Level 1 (L1) observations of  $\sigma_o$  and LES with the 10 meter referenced ocean surface wind speed ( $u_{10}$ ), as determined by Numerical Weather Prediction (NWP) models. A large population of these pairings is partitioned into “bins” with respect to  $u_{10}$  and the incidence angle ( $\theta_{inc}$ ) of the observation. The average values of  $u_{10}$  and the L1 observable within a bin are paired together as one discrete sample of the GMF for that observable. An algebraic parametric model is then fit to the discrete GMF samples to produce a continuously varying GMF which is used by the Level 2 (L2) wind speed retrieval algorithm.

### A. Description of Training Data Set: ECMWF & GDAS matchups

Matchup NWP data used to train the empirical GMF are the 10 meter referenced ocean surface wind speeds provided by the European Centre for Medium-Range Weather Forecasts (ECMWF) and the Global Data Assimilation System (GDAS). ECMWF is an independent intergovernmental organization supported by 34 countries to produce current weather forecasts and climate reanalysis products and to perform related research activities [25]. The reanalysis products are used here. GDAS is a system operated by the NOAA National Centers for Environmental Information to organize a variety of surface, balloon, aircraft and spaceborne observations into a gridded model space for use by NOAA’s global forecast system [26]. ECMWF and GDAS use a 0.25 deg and 1.0 deg reporting interval, respectively. Bilinear interpolation in space and linear interpolation in time of the reported NWP products are used to estimate  $u_{10}$  at the times and locations of the CYGNSS specular point observations.

A merged “ground truth”  $u_{10}$  product is used which combines model outputs by both ECMWF and GDAS. For

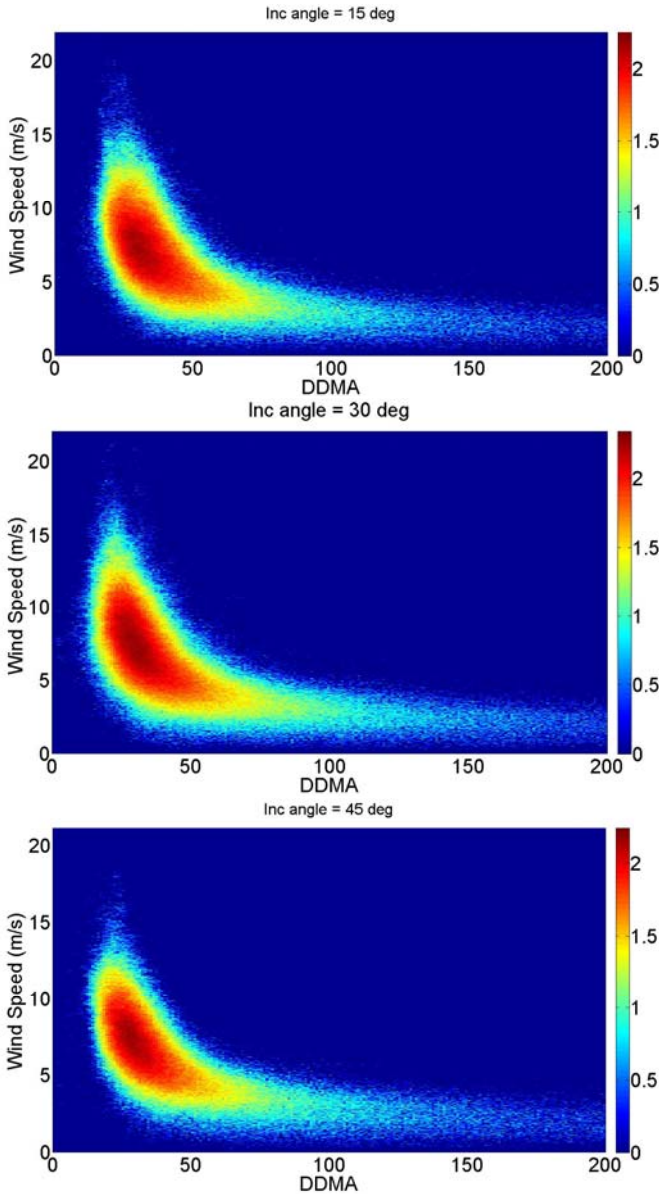


Fig. 1. Log(density) scatterplots of  $\sigma_o$  measured by CYGNSS vs. ground truth  $u_{10}$  at incidence angles of  $15^\circ$  (top),  $30^\circ$  (mid) and  $45^\circ$  (bot). The color scale is the  $\log_{10}$  of the number density of points.

wind speeds below 20 m/s, the ECMWF value for  $u_{10}$  is used alone. For wind speeds between 20 and 25 m/s, the arithmetic average of ECMWF and GDAS wind speeds is used. For wind speeds above 25 m/s, the GDAS value alone is used. This merged-product approach is used to accentuate the better accuracy of ECMWF at lower wind speeds and of GDAS at higher wind speeds [27]. In addition, matchups are only used if the  $u_{10}$  values for ECMWF and GDAS differ by no more than 3 m/s.

Examples of the training data set are shown in Fig. 1 for the  $\sigma_o$  observable at three values of  $\theta_{inc}$ . Shown are logarithmic density scatterplots of the merged ground truth  $u_{10}$  values vs. the observable. The general trend is for the scattering cross section to decrease as wind speed increases, as expected for bistatic forward scattering from a wind-roughened ocean surface.

### B. Binning of matchups for discrete, empirical GMF

The CYGNSS L1 observables are filtered prior to use as part of the training used to derive the empirical GMF. The filters are for reasons of quality control. Specifically:

- The Doppler coordinate of the specular point in the DDM is required to be greater than the lowest possible value in the map and less than the highest possible value. This discards cases where it is at the edge of the map and the computed Doppler coordinate may be incorrect. In practice, this happens less than 0.1% of the time.
- The delay coordinate of the specular point in the DDM is required to be greater than the lowest possible value in the map and less than the highest possible value. This discards cases where it is at the edge of the map and the computed delay coordinate may be incorrect. In practice, this happens less than 0.1% of the time.
- All NaN values of the observables are discarded. This eliminates samples for which noise in the calibration data can produce non-physical calibrated L1 data. In practice, this happens less than 0.1% of the time.
- The observables are required to be non-negative. This eliminates samples for which noise in the calibration data can produce non-physical calibrated L1 data, as well as measurements which are very close to the measurement noise floor. In practice, this happens less than 0.1% of the time.
- All measurements are discarded for which the spacecraft star tracker is not tracking due to solar contamination. Some reported spacecraft attitude data during sun outages are known to be erroneous (with inaccuracies greater than the error allocation in the L1 calibration algorithm for attitude knowledge). This only occurs when the outage is especially long, but all sun outage data are flagged and removed as a precaution. In practice, this happens less than 1% of the time.
- All data with a CYGNSS Range Corrected Gain (RCG) of less than 10 are discarded. RCG is a composite measure of receive signal strength that combines the receive antenna gain in the direction of the specular point with the  $R^{-2}$  propagation range loss from the GPS transmitter to the specular point and from the specular point to the CYGNSS receiver. In practice, data with an  $RCG > \sim 1$  can typically produce useful wind speed retrievals, but only data with a higher SNR are used to train the empirical GMF.
- All observations resulting from transmissions by the GPS Block Type II-F satellites are discarded. Block II-F is the newest family of GPS satellites, and the one for which the CYGNSS team has the least information about its transmitter antenna gain pattern. There are currently 8 II-F satellites in the constellation, out of 31 total in operation.

The behavior of the empirical GMF as a function of  $u_{10}$  and  $\theta_{inc}$  is smoothed by allowing sequential bins in either dimension to overlap. In the incidence angle dimension, the bin center is incremented every 1 deg from 1 to 70 deg and all

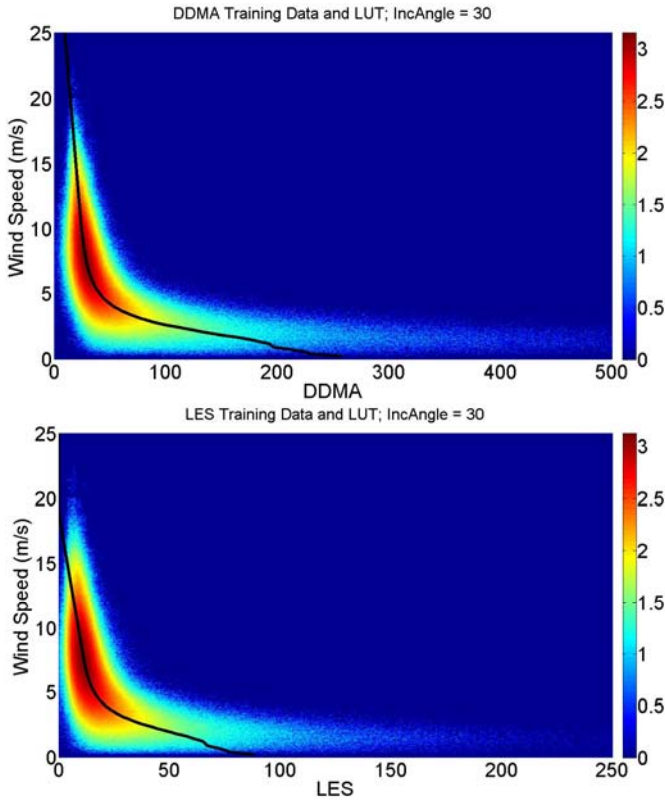


Fig. 2. Empirical GMFs for the two Level 1 observables,  $\sigma_o$  or DDMA (top) and LES (bot), at  $\theta_{inc} = 30^\circ$ , overlaid on log(density) scatter plots of the training data from which they were derived.

samples are included within  $\pm 2.0$  deg of the center. In the wind speed dimension, the bin center is incremented every 0.1 m/s from 0.05 to 34.95 m/s and all samples are included within a variable bin width that varies according to the population density of samples as a function of wind speed. Specifically, the bin widths used are:

- $\pm 0.4$  m/s ( $u_{10} < 2$  m/s)
- $\pm 0.3$  m/s ( $2 < u_{10} < 5$  m/s)
- $\pm 0.2$  m/s ( $5 < u_{10} < 9$  m/s)
- $\pm 0.4$  m/s ( $9 < u_{10} < 11$  m/s)
- $\pm 0.6$  m/s ( $11 < u_{10} < 14$  m/s)
- $\pm 0.8$  m/s ( $14 < u_{10} < 17$  m/s)
- $\pm 1.0$  m/s ( $17 < u_{10}$ )

A weighted average of all samples within twice these bin width ranges is performed. Samples within  $\pm$  one bin width of the bin center are given twice as much weight as those between  $1 \times$ binwidth and  $2 \times$ binwidth from the bin center. This tapered weighting approach reduces the introduction of artificial higher frequency components into the GMF than are present in the original discrete empirical samples.

The GMF is also forced to be monotonic as a function of wind speed. The GMF value at 7.05 m/s is computed first (since this is generally the most probable wind speed and so has the largest population of samples in its near vicinity). GMF values are then sequentially computed in steps of 0.1 m/s above and below this value using the averaging scheme described above. However, values are allowed to either decrease or stay the same with increasing wind speed, and increase or stay the same with decreasing wind speed. This

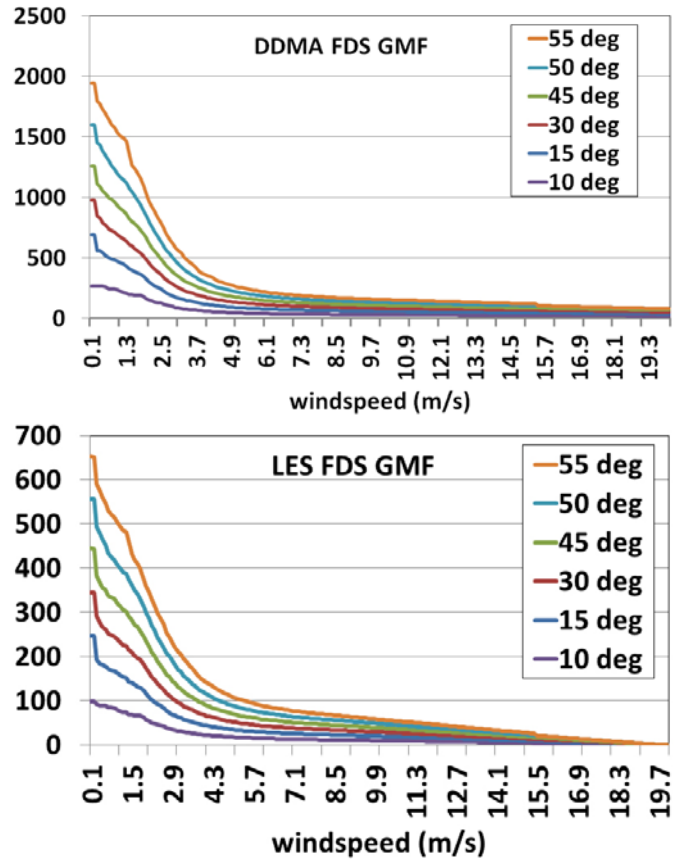


Fig. 3. Empirical GMFs for  $\sigma_o$  (top) and LES (bot) at  $\theta_{inc}=10, 15, \dots, 55^\circ$ .

limits the introduction of non-physical variations into the GMF due to undersampling of certain parts of the (wind speed, incidence angle) state space. In practice, this monotonicity algorithm is only enforced at the highest and lowest wind speeds in the population, where the sampling density tends to be lowest.

Examples of the empirical GMFs for both observables ( $\sigma_o$  and LES) at  $\theta_{inc} = 30$  deg, overlaid on the training data from which they were derived, are shown in Fig. 2. Over the central range of wind speeds where most of the samples occur, the GMF agrees with the highest density part of the scatter plot. At the highest and lowest wind speeds, the lower size of the population makes the behavior of the GMF more susceptible to errors.

Examples of the empirical GMFs for both L1 observables across a range of incidence angles are shown in Fig. 3. The general dependence of observable on wind speed is consistent across all incidence angles. The dependence on incidence angle at a given wind speed is also consistent. Note that the slope of the GMF ( $dObs/du_{10}$ ) is highest at low wind speeds, indicating that wind speed retrievals will, in general, perform better and be less susceptible to measurement noise and calibration errors at the lower wind speeds. The general behavior of the empirical  $\sigma_o$  GMF, both as a function of wind speed and of incidence angle, is consistent with scattering model predictions based on the first order small slope approximation method [28], [29].

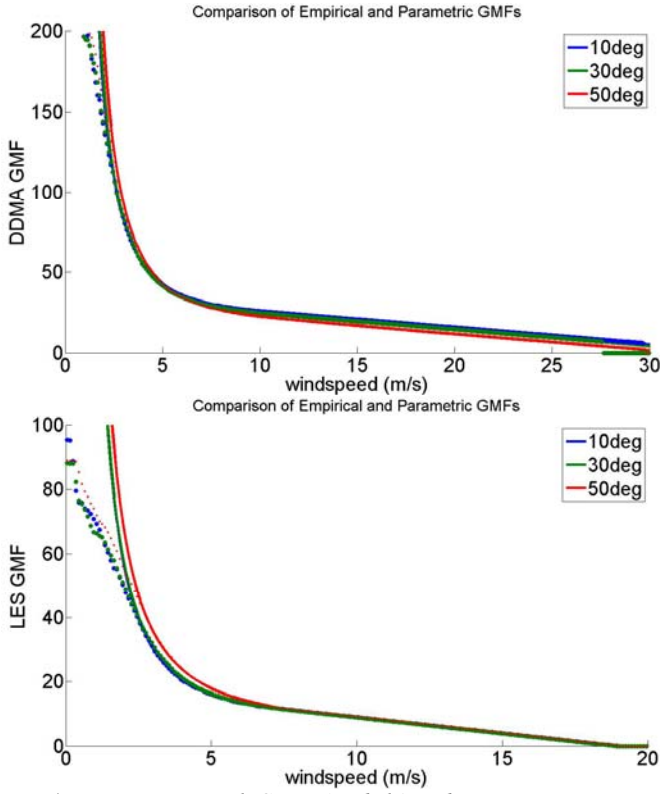


Fig. 4. Discrete empirical GMFs (symbols) and continuous parametric models (solid lines) derived from them, for the two L1 observables  $\sigma_o$  (top) and LES (bot), and for  $\theta_{inc} = 10, 30, 50^\circ$ .

### C. Parametric model for continuous, empirical GMF

An algebraic parametric model is fit in a least-squares sense to the empirical GMF in order to populate the lookup tables used by the CYGNSS Level 2 wind speed retrieval algorithm. This process smooths across some of the behavior in the empirical GMF that is related to measurement noise and insufficient number of samples in the training set. It also interpolates across portions of (wind speed, incidence angle) state space that are not sufficiently populated by the training set. The parametric model assumed for the GMF is divided into two portions based on the observed behavior of the empirical GMF as a function of wind speed. At low wind speeds, a model is assumed of the form

$$Obs = a_0 + a_1 u^{-1} + a_2 u^{-2} \quad (1)$$

where  $Obs$  is the Level 1 CYGNSS observable (either  $\sigma_o$  or LES),  $u$  is the ground truth  $u_{10}$  wind speed, and  $a_i$  are the dependent parameters of the model. At high wind speeds, a model is assumed of the form

$$Obs = b_0 + b_1 u + b_2 u^2 \quad (2)$$

where  $b_i$  are the dependent parameters of the model. The population of samples used to train these two models is different for each observable. For  $\sigma_o$ , samples at wind speeds below 15 m/s are used to determine  $a_{0-2}$  and samples above 15 m/s are used to determine  $b_{0-2}$ . For the LES observable,

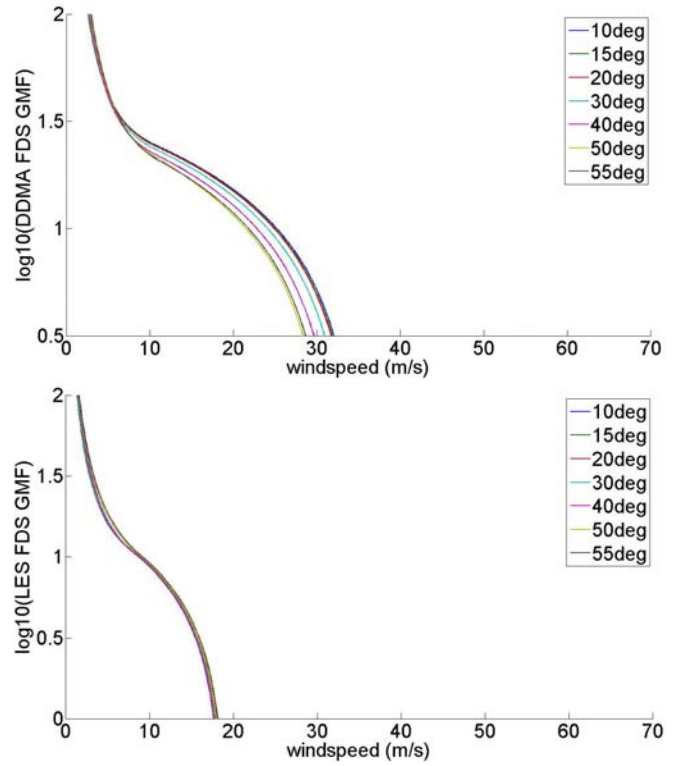


Fig. 5. Parametric model FDS GMF for the Level 1 observables  $\sigma_o$  (top) and LES (bot) at incidence angles of 10, 15, ..., 55 deg. The dependence on incidence angle is more pronounced in the case of the  $\sigma_o$  (DDMA) observable. The maximum wind speed at which the observable is sensitive to changes in wind speed is also higher for  $\sigma_o$  than for the LES observable.

samples below and above 10 m/s are used. The actual transition from one parametric model to the other in the GMF occurs near, but not exactly at, these wind speed values. A transition point is chosen where the first derivatives of the two models are equal (i.e. a spline fit). The model parameters and the spline fit transition point are chosen independently at each incidence angle.

Examples of the parametric model GMF, together with the empirical GMF from which they are obtained, are shown in Fig. 4. At the lowest wind speeds (below  $\sim 2$  m/s), the empirical and parametric models tend to deviate (more so for the LES observable). The sensitivity of the LES observable to wind speed drops to zero at wind speeds above  $\sim 18$  m/s, whereas the  $\sigma_o$  observable retains its sensitivity up to wind speeds of  $\sim 30$  m/s.

Examples of the parametric model GMFs for both observables and over a range of incidence angles are shown in Fig. 5. The truncation of the GMF at high wind speeds results from the limitations in the dynamic range of wind speeds included in the training data set.

### D. Validation and performance characterization

As a means of assessing whether the derived GMFs properly represent the response of the Level 1 observables to changes in ocean surface wind speed, they are used as the basis for a wind speed retrieval algorithm. The algorithm inverts the GMF to estimate wind speed given the measured observable [19]. The error in this retrieval algorithm (groundtruth – retrieval) is considered as a function of the two

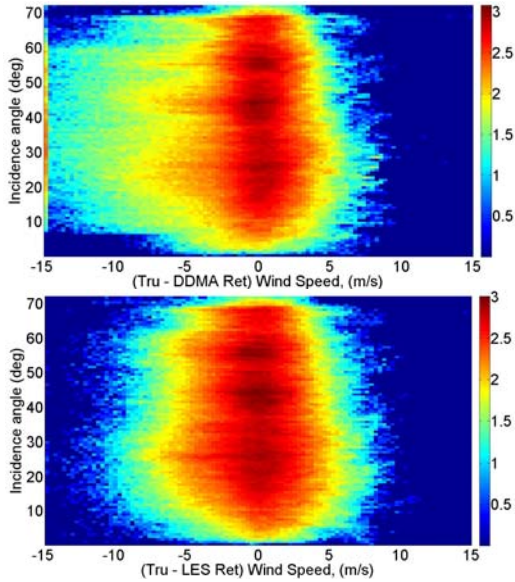


Fig. 6. Log(density) scatter plot of wind speed retrieval error vs. incidence angle for retrievals using the  $\sigma_0$  (top) and LES (bot) Level 1 observable. There is no significant dependence on incidence angle.

coordinates of the GMF, incidence angle and wind speed. Note that this comparison uses the same population of data as was used to train the GMFs and so should be considered a test of internal consistency in the generation of the GMFs. A more independent assessment of retrieval performance is presented in [30].

The dependence of retrieval error on incidence angle is shown in Fig. 6. The  $\sigma_0$ -based retrieval on the left shows a positive statistical retrieval bias (retrieved values are larger than groundtruth more often than they are smaller). The LES-based retrieval on the right shows a more unbiased distribution of retrieval errors. Notably, in terms of incidence angle dependence, the highest density of retrieval errors occurs near an error of zero and this is true at all incidence angles and for

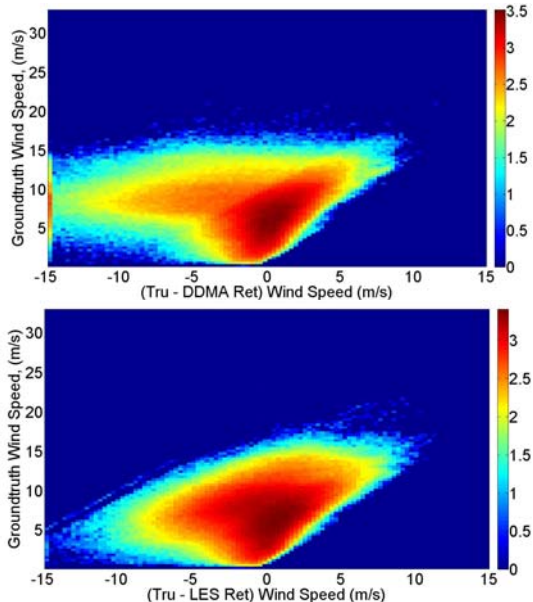


Fig. 7. Log(density) scatter plot of wind speed retrieval error vs. ground truth wind speed for retrievals using the  $\sigma_0$  (top) and LES (bot) L1 observable.

both L1 observables.

The dependence of retrieval error on the ground truth wind speed is shown in Fig. 7. Significant positive retrieval biases (retrieved values are larger than groundtruth more often than they are smaller) can be seen at ground truth wind speeds of 5-15 m/s for  $\sigma_0$  and at 3-10 m/s for LES. A possible cause for this behavior, and a corresponding mitigation strategy, are considered next.

Fig. 8 shows the dependence of retrieval error on the difference between the wind speeds retrieved using the two L1 observables. Larger retrieval errors tend to be highly correlated with the difference between the two retrievals. The large positive bias in retrievals based on the  $\sigma_0$  observable tends to coincide with cases where the  $\sigma_0$  retrieval is much larger than that from the LES observable. Alternately, samples for which the  $\sigma_0$  retrieval is much smaller than the LES retrieval tend to coincide with large positive biases in the LES retrieval. The root cause of this behavior may be related to the fact that the two observables respond to different aspects of the sea state, only part of which is forced by local wind speed. If, for example, they respond in different ways to the longer swell portion of the surface wave spectrum, this could explain their different dependence on the retrieval error. One hypothesis is that young sea conditions (not fully developed) may coincide with instances where the two retrievals have significant differences.

In terms of mitigation of this behavior, and improvement in the overall wind speed retrieval performance, the dependence of retrieval error on the difference between the  $\sigma_0$  and LES retrieved wind speeds can be used as a quality control (Q/C) filter. This is illustrated in Fig. 9, which shows the dependence of the retrieved Minimum Variance (MV) wind speed on the difference. The MV retrieval is a weighted average of the  $\sigma_0$  and LES retrievals, weighted by the inverse variance of the error in wind speed retrieved by each of the individual

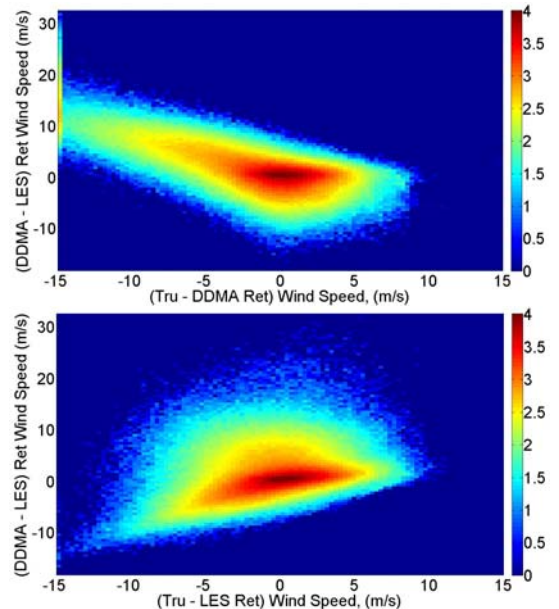


Fig. 8. Log(density) scatter plot of wind speed retrieval error using the  $\sigma_0$  (top) and LES (bot) L1 observable vs. the difference between the two retrieved wind speeds.

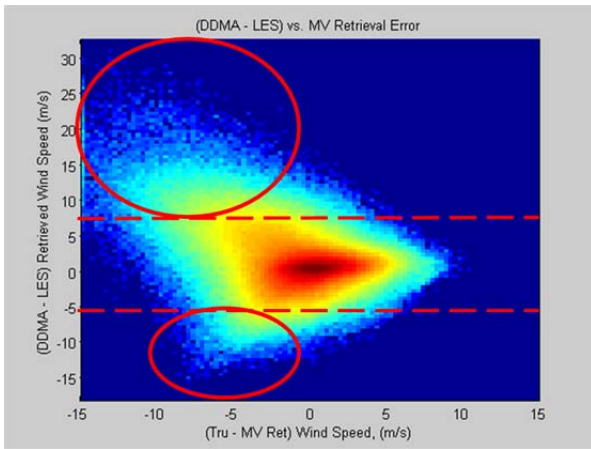


Fig. 9. Log(density) scatter plot of minimum variance wind speed retrieval error vs. the difference between the wind speeds retrieved by the two individual L1 observables. A Q/C filter that discards retrievals with differences greater than 6 m/s (shown by the two dashed red lines) will eliminate the circled regions with large retrieval errors.

observables [19]. Large errors in the MV retrieval can be seen in Fig. 9 to correlate with large differences between the  $\sigma_0$  and LES retrievals. A simple Q/C filter could, for example, exclude all retrievals for which the difference is greater than 6 m/s. This filter threshold is illustrated in Fig. 9. In practice, this Q/C filter discards approximately 4% of the samples.

The effectiveness of the Q/C filter, and the overall quality of the MV retrieval algorithm, is illustrated in Fig. 10, which compares the groundtruth and retrieved wind speeds as a scatter plot and by their RMS and mean difference. The large retrieval biases evident in Fig. 7 have been largely removed by this Q/C filter. Fig. 10 also illustrates the performance of the wind speed retrieval below 20 m/s. The RMS difference is  $\sim 2$

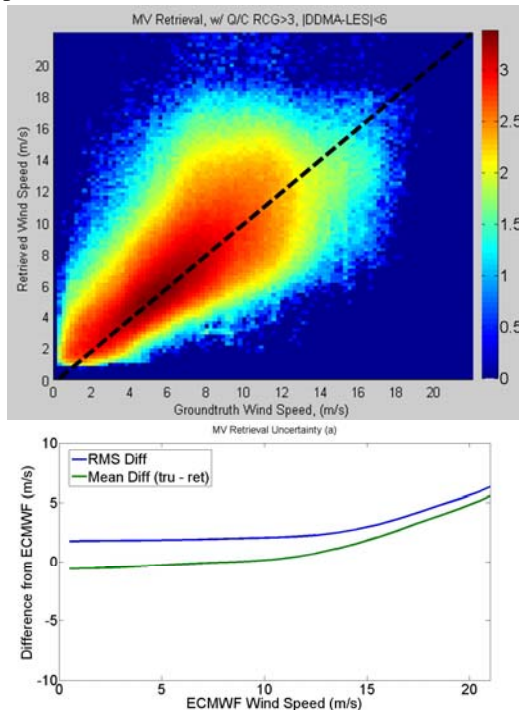


Fig. 10. Log(density) scatter plot of groundtruth vs. MV retrieved wind speed (top) with black-dashed line of 1:1 agreement, and of RMS and mean retrieval error vs. groundtruth wind speed (bot).

m/s at low wind speeds and grows to  $\sim 4$  m/s at 20 m/s.

### III. YOUNG SEAS/LIMITED FETCH GMF

The YSLF GMF is based on matchups between measurements by CYGNSS made during overpasses of 2017 Atlantic hurricanes and near-coincident ocean surface wind speed measurements made by the Stepped Frequency Microwave Radiometer (SFMR) on NOAA P-3 hurricane hunter aircraft [24]. These matchups demonstrate a fairly consistent sensitivity of the CYGNSS L1 observables to changes in wind speed at high (30-60 m/s) levels. The mean high wind sensitivities ( $d\sigma_0/du_{10}$  and  $dLES/du_{10}$ ) are used to define a YSLF GMF that is consistent with the fully developed seas GMF at low wind speeds but whose high wind behavior is replaced by the YSLF sensitivities derived from the SFMR matchups over hurricanes.

#### A. Description of Training Data Set: NOAA P-3 SFMR matchups

Twenty-five (25) coincident overpasses of hurricanes between CYGNSS and NOAA P-3 aircraft occurred during the 2017 Atlantic hurricane season. Coincidence was defined by locating the aircraft ground track during one of its eyewall penetrations that was closest to a CYGNSS specular point track for that overpass and requiring that they occurred within 60 min of one another. The 25 cases identified in this way include overpasses of Hurricanes Harvey, Irma and Maria. The maximum SFMR wind speed recorded across all cases was 73 m/s and the range of CYGNSS incidence angles covered 13-67 deg. Histograms of the SFMR  $u_{10}$ , CYGNSS  $\theta_{inc}$ , and CYGNSS  $\sigma_0$  measured across all 25 overpasses are shown in Fig. 11.

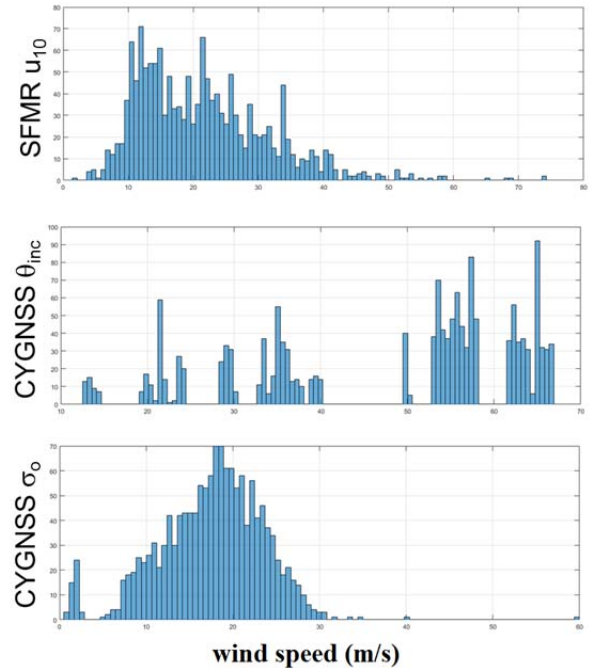


Fig. 11. Histograms of the SFMR  $u_{10}$ , CYGNSS  $\theta_{inc}$ , and CYGNSS  $\sigma_0$  measured across all 25 coincident hurricane overpasses that are used to determine the high wind portion of the limited fetch GMF.

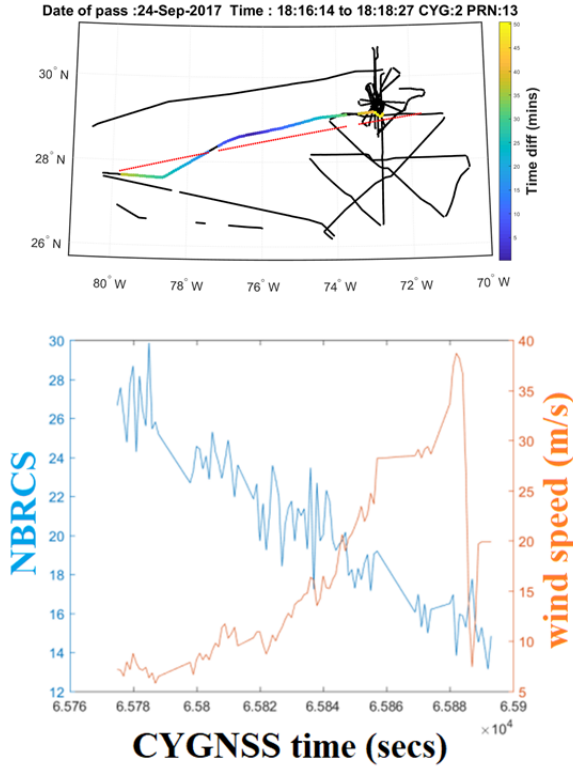


Fig. 12. Coincident CYGNSS/P-3 overpass of Hurricane Maria on 24 Sep 2017 at 1817 UTC. (top) The P-3 ground track is shown in black. The CYGNSS specular point track is shown in red. The colored portion of the P-3 track is color coded by their time difference. (bot) CYGNSS L1  $\sigma_0$  (labeled NBRCS) and SFMR wind speed measured along the coincident track.

An example of one of the coincident overpasses, occurring over Hurricane Maria on 24 Sep 2017, is shown in Fig. 12. The CYGNSS measurement of  $\sigma_0$  can be seen to decrease roughly monotonically as the wind speed measured by SFMR increases.

### B. Regression of coincident overpasses to determine GMF sensitivity ( $d\sigma_0/du_{10}$ )

For each of the 25 coincident hurricane overpasses, the L1 observables are related to the coincident SFMR wind speeds by linear regression. One example of this is shown in Fig. 13, for the case illustrated in Fig. 12. The slope of the linear regression is taken as the sensitivity of the observable to changes in wind speed.

Fig. 14 shows the slope of the linear regression determined for each of the 25 cases and for both L1 observables. The set of all 25 regression slopes is averaged together to determine the sensitivity of the YSLF GMF. The resulting sensitivity factors are

$$\begin{aligned} d\sigma_0/du_{10} &= -0.1880 \text{ (m/s)}^{-1} \\ dLES/du_{10} &= -0.0929 \text{ (m/s)}^{-1} \end{aligned} \quad (3)$$

### C. Parametric model with hi/lo wind partitions

As with the fully developed seas GMF, an algebraic parametric model is assumed for the YSLF GMF. The parametric model is again divided into low and high wind speed portions. At low wind speeds, a similar model is assumed as for the FDS GMF

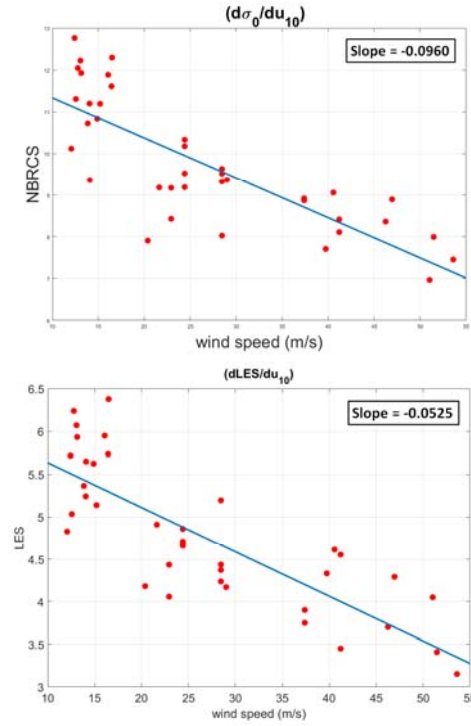


Fig. 13. Linear regression of CYGNSS L1  $\sigma_0$  and LES observables against SFMR wind speed for Hurricane Maria overpass on 24 Sep 2017 at 1817 UTC. The slope of the linear regression is noted in each plot.

$$Obs = a_0 + a_1 u^{-1} + a_2 u^{-2} \quad (4)$$

and the  $a_{0-2}$  coefficients are again determined using the fully developed seas training set. At high wind speeds, a linear model is assumed

$$Obs = c_0 + c_1 u \quad (5)$$

with slope coefficient ( $c_1$ ) given by eqn. (3) as determined from the linear regression of hurricane overpass matchups. The transition between low and high wind speed segments is again selected as the wind speed where the first derivatives of the two models are equal. The low wind speed model parameters and the spline fit transition point are chosen

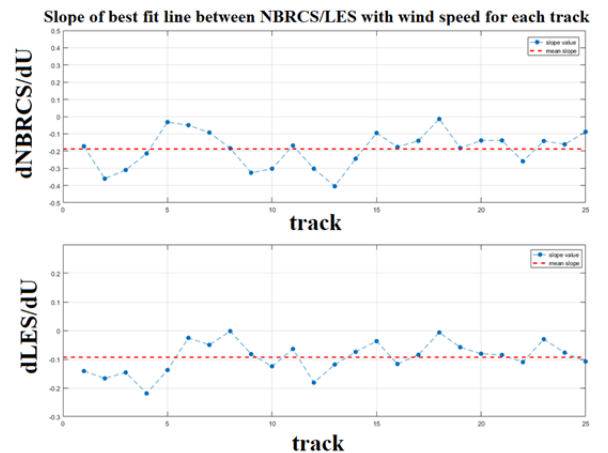


Fig. 14. Slope of the linear regression determined from each of the 25 coincident hurricane overpasses for both the  $\sigma_0$  (top) and LES (bot) L1 observable.

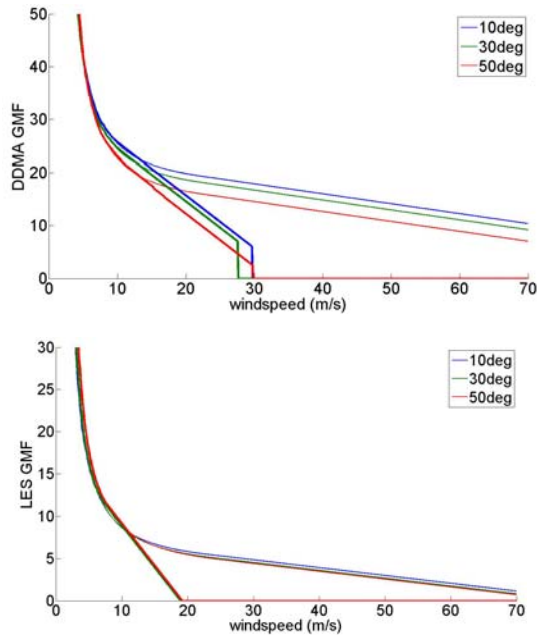


Fig. 15. Young Seas/Limited Fetch GMF (thin lines) for  $\sigma_o$  (left) and LES (right), together with the Fully Developed Seas GMF (thick lines), at  $\theta_{inc} = 10, 30, 50^\circ$ . The models agree at low wind speeds but have very different high wind speed dependencies.

independently at each incidence angle. A common high wind speed sensitivity is assumed for all incidence angles, since there was no clear dependence of sensitivity on incidence angle evident in the coincident hurricane overpass data.

Examples of the YSLF GMF are shown in Fig. 15, together with the FDS GMFs at the same incidence angles. Several characteristics are noteworthy. The models agree at low wind speeds (by design). At wind speeds in the range 15-25 m/s, the sensitivity ( $dObs/du_{10}$ ) is markedly stronger in the FDS case. The limiting wind speed, above which the value of the observable is zero, is much higher in the YSLF case. And finally, there is a range of values of both observables over

which two different wind speeds correspond to the same measurement. This represents an ill-posed, multi-valued inversion problem. In practice, it may be necessary to have some *a priori* knowledge about the fetch or sea age of the conditions under observation in order to uniquely convert L1 observable measurements to wind speed.

The multi-valued nature of the mapping from L1 observable to wind speed is illustrated in Fig. 16. The FDS and YSLF GMFs agree below  $\sim 12$  m/s. Above 12 m/s, the behavior of the FDS GMF is derived from matchups with ECMWF and GDAS away from major storms. The behavior of the YSLF GMF above 12 m/s is derived from matchups with P-3 SFMR wind speed measurements in major storms. The YSLF GMFs for both L1 observables are shown in Fig. 17.

*D. Validation and performance characterization; repeatability of limited fetch conditions*

The adequacy of the YSLF GMFs to represent the response of the Level 1 observables to changes in ocean surface wind speed in hurricanes is assessed by using it in a wind speed retrieval algorithm. The algorithm inverts the GMF to estimate wind speed given the measured observable, in the same manner as the previous assessment for the FDS GMF. In this case, given the limited number of coincident hurricane overpasses that are available, individual case studies are considered rather than overall performance statistics. The wind speed retrieval performance for each hurricane overpass is evaluated using CYGNSS/P-3 matchups similar to the one shown in Fig. 12. The retrieval results for four overpasses are shown in Figs. 18a-d, presented as a time series of the CYGNSS retrieved wind speed overlaid with the nearest SFMR and merged ECMWF&GDAS wind speeds.

In general, the lower wind speed portions of the CYGNSS tracks agree well with the ECMWF&GDAS wind speeds and the high wind speed portions near the storm center agree with the SFMR wind speeds. Note that the CYGNSS retrievals at

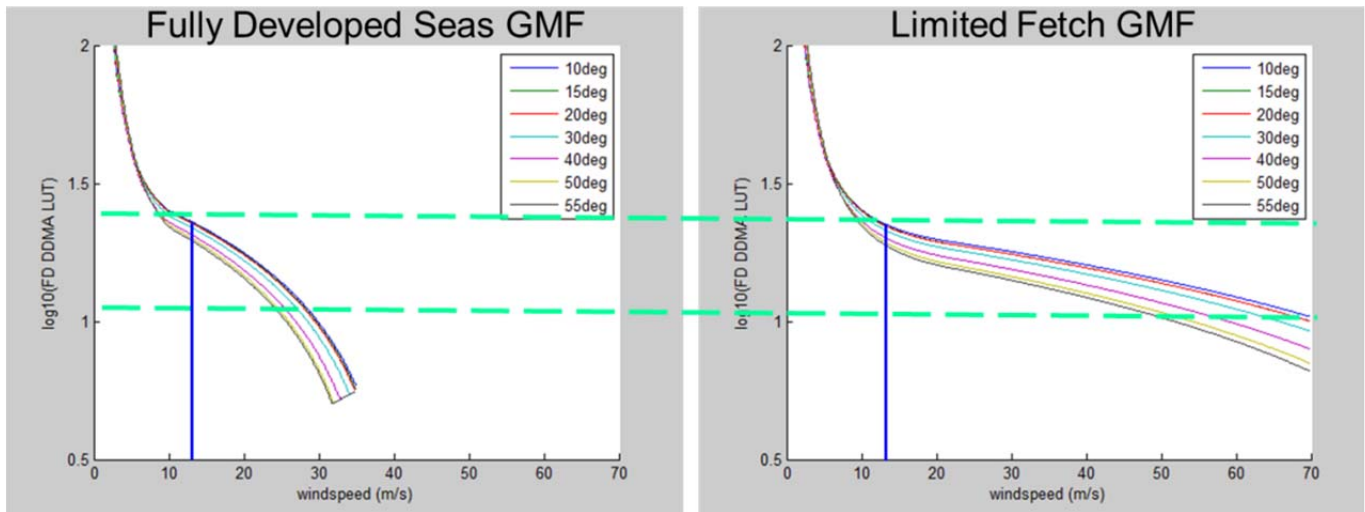


Fig. 16. Side-by-side comparison of GMFs for  $\sigma_o$  that are appropriate for Fully Developed Seas (left) and Young Seas/Limited Fetch conditions in hurricanes (right). The region of the L1 observable bounded by the two dashed green lines maps onto two distinct wind speeds from the same value of  $\sigma_o$ . The wind speed marked by the vertical blue line (12 m/s) represents the highest wind speed with a common mapping by both GMFs.

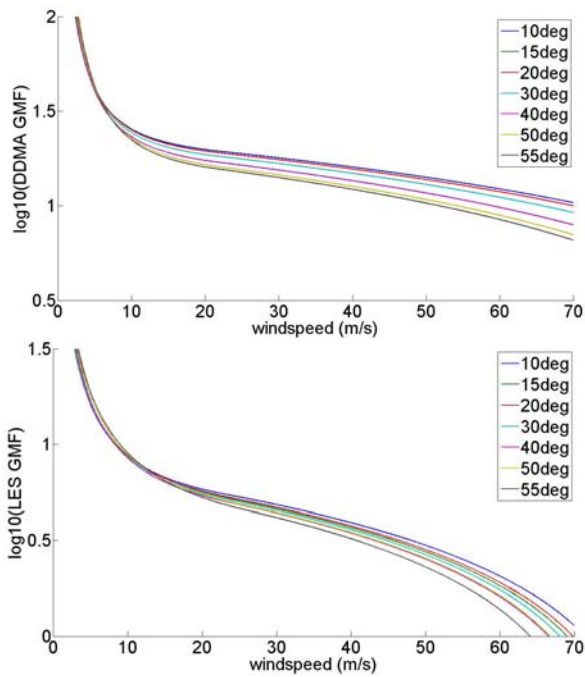


Fig. 17. Representative YSLF GMFs for the Level 1 observables  $\sigma_o$  (top) and LES (bot) at incidence angles of 10, 15, ..., 55 deg. The dependence on incidence angle is more pronounced at higher wind speeds with both observables.

the highest wind speed levels tend to be noisier, as can be expected given the lower slope of the GMF at high wind speeds. The wind speed retrieved by CYGNSS using the FDS GMF is also included in Fig 18 for comparison. The CYGNSS YSLF and FDS winds agree closely at low wind speed speeds, which is consistent with their very similar GMFs at low winds. At high wind speeds, the YSLF retrievals are higher than the FDS ones, which is also consistent with the higher values for  $\sigma_o$  in the YSLF than the FDS GMF at the same wind speed (see Fig. 16). Occasional drop-outs in the reported FDS winds are evident in Fig. 18 near the storm center. They result from quality control filters which flag the retrievals as unreliable when the individual FDS DDMA and LES retrievals differ by more than 6 m/s.

#### IV. DISCUSSION

The dependence of CYGNSS measurements on the local wind speed at the location of the measurement is multi-valued in the sense that different wind speeds can result in the same values for  $\sigma_o$  and LES. The relationship appears to be strongly dependent on sea age, with fully developed seas generally exhibiting a repeatable, single-valued mapping. This is demonstrated by the RMS difference between CYGNSS retrieved winds and coincident NWP matchups. As shown in Fig. 10, the RMS difference is between 2 and 3 m/s for NWP wind speeds below 15 m/s, then begins to rise in conditions that are more likely to include partially developed seas. For the young seas with limited fetch that are more typical of conditions in and near tropical cyclones, coincident matchups with airborne SFMR measurements indicate significantly higher values for the  $\sigma_o$  and LES measurements than are

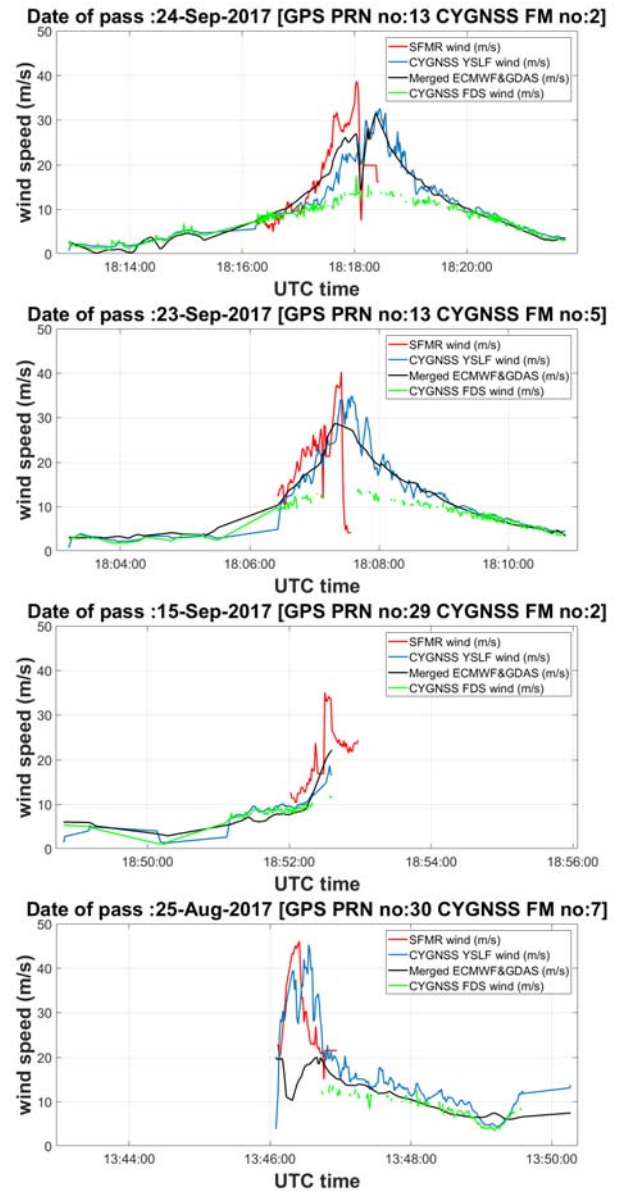


Fig. 18. Coincident hurricane overpasses by CYGNSS and underflights by the NOAA P-3 hurricane hunter aircraft of: (a) Hurricane Maria on 24 Sep 2017, 1817 UTC; (b) Hurricane Maria on 23 Sep 2017, 1807 UTC; (c) Hurricane Maria Coincident Overpass on 15 Sep 2017, 1852 UTC; and (d) Hurricane Harvey on 25 Aug 2017, 1346 UTC. Four wind products are shown: CYGNSS FDS and YSLF retrievals, Stepped Frequency Microwave Radiometer (SFMR) on the P-3 aircraft, and merged numerical weather predictions by ECMWF and GDAS models.

observed in the fully developed seas cases, given the same wind speed. This general trend continues for matchups near the inner core of the tropical cyclones, at wind speed values which are above those reported by NWP models.

A detailed assessment and characterization of the performance of a CYGNSS wind speed retrieval algorithm based on the GMF developed here is reported in [30]. To evaluate performance below 20 m/s, a large (~30 million) population of retrieved winds using the FDS GMF is compared to near-coincident winds reported by ECMWF. The RMS difference between them is found to be 2.0 m/s and the component of that difference due to uncertainty in the CYGNSS wind speed retrieval is estimated to be 1.4 m/s.

Above 20 m/s, performance is evaluated by comparisons between winds retrieved using the YSLF GMF and near-coincident winds measured by the SFMR instrument on the P-3 hurricane hunter aircraft during eyewall penetrations. In this case, the population of intercomparisons contains 674 samples. The RMS difference between samples is found to be 6.5 m/s and the component of the difference ascribed to uncertainty in the CYGNSS retrievals is 5.0 m/s. The significantly larger uncertainty in CYGNSS retrievals at high wind speeds is believed to result from two primary causes. One is the decrease in sensitivity of the L1 observables to changes in wind speed as the winds increase. This is illustrated in Fig. 16 by the decrease in slope of both the FDS and YSLF GMFs as wind speed increases. A second cause for the increased retrieval uncertainty at high winds is the sensitivity of the L1 observables to sea state conditions not directly related to wind speed – in particular, to sea age or fetch length in and near tropical cyclones.

The multi-valued dependence on wind speed can be explained by considering the general relationship between GNSS-R measurements and sea state, and the relationship between the sea state at a particular location and the local wind speed there. In general, local winds tend to generate surface roughness nearly instantaneously at the smaller, capillary, wavelength end of the surface height spectrum. The influence of winds on the longer wavelength, swell, portion of the spectrum takes longer to develop, both in time and in fetch length. For this reason, young seas in limited fetch conditions will tend to have a smaller long wave portion of their spectrum. In fully developed seas, the wind speed has sufficient time to influence the full roughness spectrum and the relationship between capillary and swell waves is more consistent. This general behavior is consistent with the fact that the derived empirical GMFs map values for  $\sigma_0$  and LES to higher wind speeds in young sea/limited fetch conditions than in fully developed seas.

The existence of multiple GMFs presents implementation challenges for a wind speed retrieval algorithm in terms of deciding which one to use and under what conditions. Use of the FDS version appears to perform well in most cases away from major storms. Likewise, the YSLF version performs well with most coincident hurricane overpass cases, but not all. The use of a single non-FDS GMF should be considered an approximation to the true dependence of the GMF on sea age or fetch length. It reflects an effective average of the relationship between L1 observables and sea state across the young seas/limited fetch conditions that were present in the 2017 Atlantic hurricanes from which the GMF was derived. A more accurate accounting for the departure from a fully developed sea state might, for example, use a fetch-dependent parametrization of the YSLF GMF, or it might modify the L1 observables based on sea age or fetch length in order to estimate an effective FDS values. These are possible improvements that are under consideration for future development of the GMF.

Rather than attempting to make corrections to the wind speed retrieval algorithm, to account for the sensitivity of the

L1 measurements to other aspects of the sea state than those directly forced by local wind speed, an alternative approach might be to directly assimilate the L1 measurements into a coupled wind/wave model that is able to predict GNSS-R measurements given a known sea state using an appropriate rough surface scattering model. Direct data assimilation has proven useful in other situations in which measurements are not uniquely determined by a single geophysical parameter, and this may be the case here as well.

## REFERENCES

- [1] Wilheit, T.T., "A Model for the Microwave Emissivity of the Ocean's Surface as a Function of Wind Speed," *IEEE Trans. Geosci. Remote Sens.*, 17(4), 244-249, DOI: 10.1109/TGE.1979.294653, 1979.
- [2] Chang, P.S., L. Li, Wilheit, T.T., "Ocean surface wind speed and direction retrievals from the SSM/I," *IEEE Trans. Geosci. Remote Sens.*, 36(6), 1866-1871, DOI: 10.1109/36.729357, 1998.
- [3] Gaiser, P. W., et al., "The WindSat spaceborne polarimetric microwave radiometer: Sensor description and early orbit performance," *IEEE Trans. Geosci. Remote Sens.*, 42, 2347-2361, doi:10.1109/TGRS.2004.836867, 2004.
- [4] Hersbach, H., A. Stoffelen, S. de Haan, "An improved C-band scatterometer ocean geophysical model function: CMOD5," *J. Geophys. Res.: Oceans*, 112(C3), doi: 10.1029/2006JC003743, 2007.
- [5] Ricciardulli, L., F. J. Wentz, "A Scatterometer Geophysical Model Function for Climate-Quality Winds: QuikSCAT Ku-2011," *J. Oceanic Atmos. Tech.*, 32, 1829- 1846, doi:10.1175/JTECH-D-15-0008.1, 2015.
- [6] Chelton D. B., and P. J. McCabe, "A review of satellite altimeter measurement of sea surface wind speed: with a proposed new algorithm," *J. Geophys. Res.*, 90(C3), 4707-4720, 1985.
- [7] Glazman, R. E., A. Greysukh, "Satellite Altimeter Measurements of Surface Winds," *J. Geophys. Res.: Oceans*, 98(C2) 2475-2483, 1993.[7] Gleason, S., "Space-Based GNSS Scatterometry: Ocean Wind Sensing Using an Empirically Calibrated Model," *IEEE Trans. Geosci. Remote Sens.*, 51(9), doi: 10.1109/TGRS.2012.2230401, 2013.
- [8] Clarizia, M., Gommenginger, C., Gleason, S., Srokosz, M., Galdi, C., di Bisceglie, M., "Analysis of GNSS-R delay-Doppler maps from the UK-DMC satellite over the ocean," *Geophys. Res. Lett.* 36, 2009.
- [9] Clarizia, M. P., Ruf, C., Jales, P. C. Gommenginger, "Spaceborne GNSS-R Minimum Variance Wind Speed Estimator," *IEEE Trans Geosci. Remote Sens.*, 52(11), 6829-6843, doi:10.1109/TGRS.2014.2303831, Nov. 2014.
- [10] Foti G., C. Gommenginger, P. Jales. M. Unwin, A. Shaw, C. Robertson, J. Roselló, "Spaceborne GNSS-reflectometry for ocean winds: first results from the UK TechDemoSat-1 mission," *Geophys. Res. Lett.*, 42, 5435-5441, doi: 10.1002/2015GL064204, 2015.
- [11] Soisuvarn, S., Z. Jelenak, F. Said, P. S. Chang, A. Egidio, "The GNSS reflectometry response to the ocean surface winds and waves," *IEEE J. Sel. Topics Appl. Earth Obs. Remote Sens.*, 9(10), 4678-4699, Oct. 2016.
- [12] Foti G., C. Gommenginger, M. Unwin, P. Jales, J. Tye, J. Roselló, "An assessment of non-geophysical effects in spaceborne GNSS reflectometry data from the UK TechDemoSat-1 mission," *IEEE J. Sel. Topics Appl. Earth Obs. Remote Sens.*, 10(7), 3418-3429, July 2017.
- [13] Foti, G., C. Gommenginger, M. Srokosz, "First spaceborne GNSS-Reflectometry observations of hurricanes from the UK TechDemoSat-1 mission," *Geophys. Res. Lett.*, 44, 12,358-12,366, 2017.
- [14] Garrison, J., Komjathy, A., Zavorotny, V., S.J.Katzberg, "Wind speed measurements using forward scattered GPS signals," *IEEE Trans. Geosci. Remote Sens.*, 40(1), 50-65, 2002.
- [15] Katzberg, S. J., R.A. Walker, J. H. Roles, T. Lynch, P. G. Black, "First GPS signals reflected from the interior of a tropical storm: Preliminary results from hurricane Michael," *Geophys. Res. Lett.*, 28, 1981-1984, 2001.
- [16] Zavorotny, V., Voronovich, A., "Scattering of GPS signals from the ocean with wind remote sensing applications," *IEEE Trans. Geosci. Remote Sens.*, 38(2), 951-964, 2000.
- [17] Katzberg, S. J., O. Torres, G. Ganoë, "Calibration of reflected GPS for tropical storm wind speed retrievals," *Geophys. Res. Lett.*, 33, L18602, doi:10.1029/2006GL026825, 2006.

- [18] Clarizia, M. P., and C. S. Ruf, "On the Spatial Resolution of GNSS-Reflectometry," *IEEE Geosci. Remote Sens. Ltrs.*, doi:10.1109/LGRS.2016.2565380, 2016.
- [19] Clarizia, M. P., and C. S. Ruf, "Wind Speed Retrieval Algorithm for the Cyclone Global Navigation Satellite System (CYGNSS) Mission," *IEEE Trans Geosci. Remote Sens.*, 54(8), doi:10.1109/TGRS.2016.2541343, Aug. 2016.
- [20] Ruf, C. S., R. Atlas, P. S. Chang, M. P. Clarizia, J. L. Garrison, S. Gleason, S. J. Katzberg, Z. Jelenak, J. T. Johnson, S. J. Majumdar, A. O'Brien, D. J. Posselt, A. J. Ridley, R. J. Rose, V. U. Zavorotny, "New Ocean Winds Satellite Mission to Probe Hurricanes and Tropical Convection," *Bull. Amer. Meteor. Soc.*, doi:10.1175/BAMS-D-14-00218.1, 385-395, Mar 2016.
- [21] Ruf, C., M. Unwin, J. Dickinson, R. Rose, D. Rose, M. Vincent, A. Lyons, "CYGNSS: Enabling the Future of Hurricane Prediction," *IEEE Geosci. Remote Sens. Mag.*, 1(2), 52-67, doi: 10.1109/MGRS.2013.2260911, 2013.
- [22] Unwin, M., M. Brummitt, C. Ruf, "The SGR-ReSI and its Application for GNSS Reflectometry on the NASA EV-2 CYGNSS Mission", *IEEE Aerospace Conference, Big Sky, Montana, March 2013*.
- [23] Clarizia, M. P., C. Ruf, P. Jales, C. Gommenginger, "Spaceborne GNSS-R Minimum Variance Wind Speed Estimator," *IEEE Trans Geosci. Remote Sens.*, 52(11), 6829-6843, doi:10.1109/TGRS.2014.2303831, Nov. 2014.
- [24] Uhlhorn, E. W., P. G. Black, J. L. Franklin, M. A. Goodberlet, J. R. Carswell, A. S. Goldstein, "Hurricane surface windmeasurements from an operational stepped frequency microwave radiometer," *Mon. Wea. Rev.*, 135, 3070-3085, doi:10.1175/MWR3454.1, 2007.
- [25] Andersson, E., A. Persson, I. Tsonevsky, *User Guide to ECMWF Forecast Products, ECMWF, v2.1, 121 pp, 2015*.
- [26] NOAA, National Centers for Environmental Information, *Global Data Assimilation System*, <https://www.ncdc.noaa.gov/data-access/model-data/model-datasets/global-data-assimilation-system-gdas>, 2018.
- [27] Jelenak, Z., personal communication, 2017.
- [28] Zavorotny, V. U., and A. G. Voronovich, "Recent progress on forward scattering modeling for GNSS reflectometry," *International Geoscience and Remote Sensing Symposium (IGARSS)*, Quebec, CANADA, 3814-3817, doi: 10.1109/IGARSS.2014.6947315, July 2014.
- [29] Ruf, C., P. Chang, M.P. Clarizia, S. Gleason, Z. Jelenak, J. Murray, M. Morris, S. Musko, D. Posselt, D. Provost, D. Starkenburg, V. Zavorotny. *CYGNSS Handbook*, Ann Arbor, MI, Michigan Pub., ISBN 978-1-60785-380-0, 154 pp, 1 Apr 2016.
- [30] Ruf, C., S. Gleason, D. S. McKague, "Assessment of CYGNSS Wind Speed Retrieval Uncertainty," *IEEE J. Sel. Topics Appl. Earth Obs. Remote Sens.*, this issue, in press.



**Chris Ruf** (SM'85–M'87–SM'92–F'01) and received the B.A. degree in physics from Reed College, Portland, OR, and the Ph.D. degree in electrical and computer engineering from the University of Massachusetts at Amherst. He is currently Professor of atmospheric science and space

engineering at the University of Michigan; and Principal Investigator of the NASA Cyclone Global Navigation Satellite System mission. He has worked previously at Intel Corporation, Hughes Space and Communication, the NASA Jet Propulsion Laboratory, and Penn State University. His research interests include GNSS-R remote sensing, microwave radiometry, atmosphere and ocean geophysical retrieval algorithm development, and sensor technology development. Dr. Ruf is a member of the American Geophysical Union (AGU), the American Meteorological Society (AMS), and Commission F of the Union Radio Scientifique Internationale. He is former Editor-in-Chief of the *IEEE Transactions on Geoscience and Remote Sensing* and has served on the editorial boards of *Radio Science* and the *Journal of Atmospheric and Oceanic Technology*. He has been the recipient of four NASA Certificates of Recognition and seven NASA Group Achievement Awards, as well as the 1997 TGRS Best Paper Award, the 1999 IEEE Resnik Technical Field Award, the 2006 IGARSS Best Paper Award, and the 2014 IEEE GRSS Outstanding Service Award.



**Rajeswari Balasubramaniam** received her B.E degree in Electrical and Electronics Engineering from Anna University, India, in 2014 and M.E degree in Geoinformatics with a specialization in Remote Sensing and Image Processing from Indian Institute of Space Science and Technology, India in 2016. She is currently a PhD student in the Climate and Space Sciences and Engineering Department at the University of Michigan, Ann Arbor, USA. Her current work focuses on various aspects of calibration and validation for the NASA Cyclone Global Navigation Satellite System mission. Her research is focused on GNSS-Reflectometry, Statistical Signal Processing, Remote Sensing Inversion Theory, Data Analysis and Microwave Engineering. She is also a member of American Geophysical Union (AGU) and IEEE Geoscience and Remote Sensing Society (GRSS)